Flow Turbulence Combust (2016) 97:27–44
DOI 10.1007/s10494-015-9674-5

Investigation on Secondary Flow Characteristics in a Curved Annular Duct with Struts

H. X. Bu[1] · H. J. Tan[1] · H. Chen[1] · X. M. He[1]

Received: 26 May 2015 / Accepted: 16 October 2015 / Published online: 31 October 2015

Abstract Under the influence of duct curvature, cross-sectional area variation and internal struts, the internal flow field within a curved annular duct becomes rather complicated and contains strong secondary flow. In this paper, the secondary flow characteristics in an annular duct with struts are experimentally and numerically investigated. The results show that large pressure gradients exist on the bends of hub and shroud. Meanwhile, two counter-rotating vortex pairs appear both along the hub-side and shroud-side surfaces. The hub-side vortex pair of which the vortex cores travel downstream parallelly evolves from the horseshoe vortex which is induced by the leading edge of the upstream strut, whereas the shroud-side vortex pair originates from the strut trailing edge and the corresponding vortex cores develop in a divergent way. Additionally, the effects of the duct exit Mach number on the secondary flow characteristics are also studied. As the exit Mach number increases, the streamwise pressure gradients increase and lead to more intense vortices, higher total pressure loss and larger flow distortion.

Keywords Secondary flow · Curved annular duct · Strut · Vortices · Pressure gradient

1 Introduction

Curved annular ducts are widely existed in airbreathing propulsion systems, taking the forms of subsonic diffusers of supersonic axisymmetric inlets[1, 2], core flow passages

✉ H. J. Tan
thj@263.net

[1] Jiangsu Province Key Laboratory of Aerospace Power System, Nanjing University of Aeronautics and Astronautics, 210016 Nanjing, People's Republic of China

of integral particle separators in turboshaft engines[3–6] and S-shaped intermediate ducts in compressor[7–9] or turbine[10–12] of turbofan engines. Taking structural demands into account, multiple struts are often circumferentially equispaced in the ducts. Consequently, the struts will inevitably interfere the internal flow, leading to complex flow phenomena, such as vortices and wakes. This not merely deteriorates the flow structures in the duct, but degrades the entire propulsion system performance as well. Therefore, the secondary flow characteristics within a curved annular duct with struts are meaningful to the advancement of the airbreathing propulsion technology.

After numerous numerical and experimental studies during the past decades, the secondary flow characteristics in the vicinity of the fins mounted on a flat plate are now clear [13–16]. However, in the curved annular ducts with struts, the internal flowfield is rather complicated due to the influence of the duct curvature and the cross-sectional area variation. Thus, it has drawn lots of research interests. In some reported papers, the curved duct was simplified without any struts [7, 17, 18]. Hu et al. [17, 18] investigated the complex flowfiled under the influence of the inlet swirl within an unstrutted inter-turbine duct (ITD). They concluded that the inner flow development was dominated by the hub-side and shroud-side counter-rotating vortices as well as the three-dimensional boundary layer separations. The vortex intensity was significantly influenced by the inlet swirl distributions due to the alteration of the boundary layer separations scale and radial pressure gradient. However, without any struts, the effect of struts on the secondary flow was uncovered. Bailey [19] investigated a curved annular duct with a single strut, pointing out that the presence of the strut had a notable effect on the flowfield and performance of the duct. Obviously, the duct they studied was still quite dissimilar to the real geometry condition. For a more realistic case with multiple struts, Sonoda et al. [20] explored the influence of downstream passage (straight and curved passages) on the inner flow. Flow patterns of the horseshoe vortex induced by the strut leading edge were both observed on the hub and shroud surfaces in two cases. In the case with the straight downstream passage, the horseshoe vortices of both sides evolved into large vortical regions of high total pressure loss, whereas in the case of the curved downstream passage, the vortical regions were clearly revealed only near the hub side. They explained that this discrepancy should originate from the difference of the streamwise pressure gradients near the duct exit between two cases. In their following study [21], the inlet boundary layer (IBL) thickness was found to have a significant impact on the hub-side vortices. At the condition of thin IBL, a single vortex was captured near the hub at the duct exit, while a vortex pair was noticeable for the thick IBL condition. However, the value of "net" total pressure loss was not significantly increased. Imperfectly, their researches were mainly concentrated on the effects of the inlet and outlet conditions on the inner flowfield within the S-shaped annular duct, lacking an in-depth study on the generation mechanism and evolution characteristics of the vortices. According to the above discussion, it is evident that the real curved annular ducts are usually coupled with struts of which the interacting flowfield is very complicated that the current published literature offers limited knowledge directly on the secondary flow characteristics.

The current paper is devoted to investigating the complex flowfield within a curved annular duct which is closed to the real geometry condition, and trying to clarify the generation and evolution of the strut-induced vortices. Besides, the effects of the exit Mach number on the secondary flow characteristics are also examined.

2 Experimental Setup

2.1 Description of the test bed

The test model is conducted on the air-suction test bed of Nanjing University of Aeronautics and Astronautics. As shown in Fig. 1, the test facility consists of a test model, a pressure measurement system, a flow meter, a pressure regulating valve and a vacuum tank with pump units. The test model is connected with the flow meter, both of which are fixed on the test bed. The pressure regulating valve is assembled downstream to control the operating condition by changing the captured mass flow rate During the test, the vacuum pumps operate continuously to create a low and stable pressure condition in the vacuum tank. Thus, the ambient air is sucked into the test model because of the low back pressure. When the flow rate reaches the required value and keeps stable, the measurement and control system begin to operate

2.2 Description of the test model

As shown in Fig. 2, the test model consists of a shroud and a hub For structural supports, eight struts, including four thick and four thin ones, are interlacedly distributed in the circumferential direction between station 1-1 and station 2-2. Figures 3 and 4 also present the configurations of the duct and the thick strut The axial length of the curved annular duct (l_0) is 92mm. The nondimensional radius change ($\Delta R/l_0$) is set to 0.41, which depicts the severity of the duct curvature. The inlet-to-exit area ratio (A_1/A_2), which determines the bulk deceleration (or acceleration) of the fluid, is 1.04. The thick strut thickness-to-chord ratio (w/l_c) is 0.17, which is twice of that of the thin ones The other geometrical parameters are listed in Table 1. In addition, Fig. 5 shows the duct area distributions for the strutted and unstrutted cases, where the x-axis and y-axis are normalized byl_0 and A_2, respectively Two monitor planes are defined at stations 1-1 and 2-2, which correspond to the inlet and exit sections of the annular duct Moreover, an inlet contraction duct with a dimensionless lengthl_1/l_0 of 2.0 and an exit diffusion duct with l_2/l_0 of 1.7 are placed upstream and downstream of the test model, respectively, to guide and adjust the duct flow In the current study, the original point of the coordinate system is set at the center of the inlet section (station 1-1).

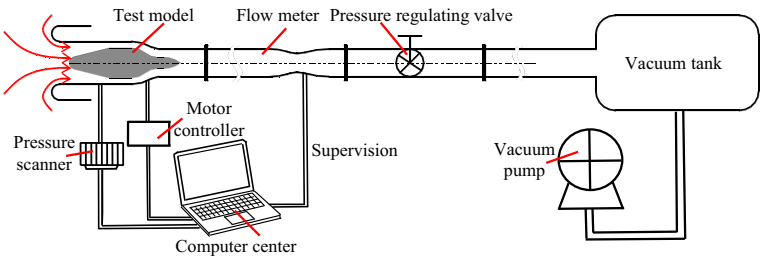

Fig. 1 Sketch of the test bed

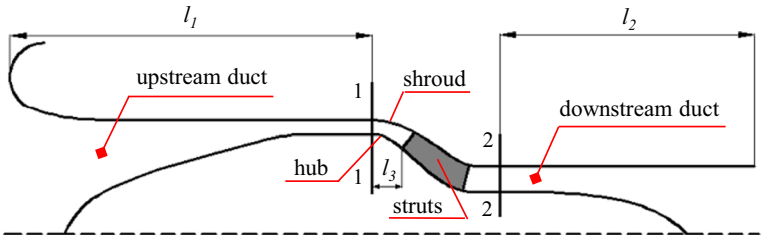

Fig. 2 Sketch of the 2-D flow path of the curved annular duct

Besides the geometrical features of the test model, Fig. 3 also exhibits the arrangement of the pressure taps Twenty pressure taps at intervals of 5.7 mm are placed along the hub and 21 pressure taps at intervals of 5.4 mm are placed along the shroud to acquire the pressure distributions within the curved annular duct The circumferential position of these taps corresponds to the middle line between two adjacent struts. In addition, on the strut surface, three rows of pressure taps are located at 10 %, 50 %, and 90 % spanwise positions, respectively Each row contains eight pressure taps which are placed at intervals of 5.5mm To obtain the total pressure distribution at the inlet section, two movable pitot tubes driven by linear electric motors are placed at station 1-1. The motion distance of the pitot tubes jointly covers the entire passage height. All the pressure signals are recorded by the PSI 9816 pressure scanner.

2.3 Description of the measurements

The measurement and control system is shown in Fig. 6, which consists of a PSI 9816 pressure scanner, a BYM-JD Venturi tube with its data acquisition system, and two linear electric motors with their control system. The pressure scanner is used to obtain the total and static pressure data. The modules with a measurement range of 15 psi are chosen, by which all the acquired pressure data have a margin error of 0.05 % FS over the full range of calibration. Moreover, the Venturi tube is introduced to measure the mass flow rate, which has a range of 1.2 kg/s with an accuracy of 0.1 % FS. To scan the total pressure profile of the inlet boundary layer, two linear electric motors are used to drive the pitot tubes to move rapidly and accurately.

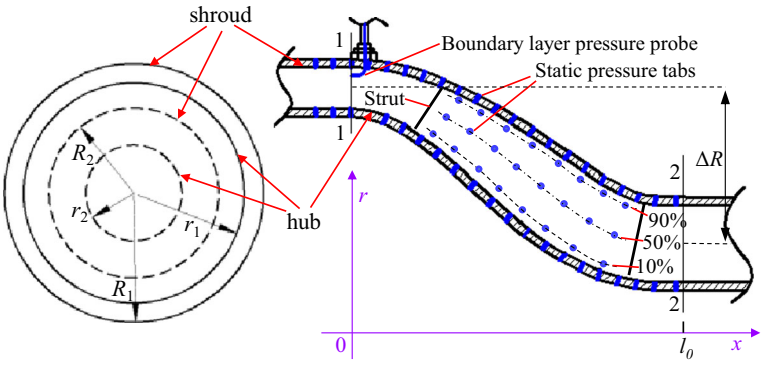

Fig. 3 Main geometrical parameters of the curved duct

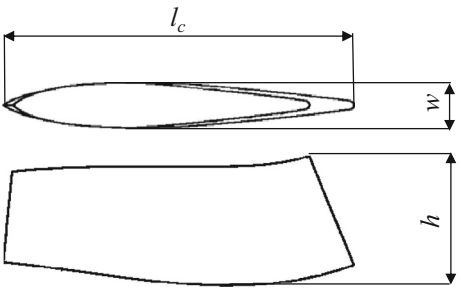

Fig. 4 Geometrical parameters of the struts

3 Numerical Approach

To obtain more details on the flow structures within the strutted curved annular duct, computational investigations are performed additionally. The computations are accomplished by the commercial CFD software ANSYS®Fluent 14.0, which uses finite volume method to solve the compressible Reynolds-Averaged Navier-Stokes (RANS) equations. The discretization of the governing equations is performed by the second-order upwind method and the Roe-scheme is applied for the approximation of the convective flux splitting. In addition, the turbulent flow is modeled by Realizable $k-\varepsilon$ model. The computational domain and the boundary conditions involved in the simulation are shown in Fig. 7. Since the geometrical shape and the flow conditions are both symmetrical about the horizontal plane and the vertical plane, the computational domain is chosen as just quarter of the actual one. Besides, a straight duct, whose length is 30 % of l_0, is extended upstream from the station 1-1. The boundary condition types include pressure-inlet, pressure-outlet, symmetry, and non-slip adiabatic wall boundary conditions. For the pressure-inlet boundary, the parameters are defined by the one-seventh-power law, while those of the pressure-outlet boundary are adapted to achieve the required mass flow rate. The convergence of each run is decided according to the residual history of each governing equation and some monitored parameters on the outlet cross section. When the residual of each equation drops six orders of magnitude and the mass flow rate along with the mass-averaged Mach number as well as the static pressure on the outlet cross section are stable, the calculation is considered converged.

The computational grid for the strutted curved annular duct is shown in Fig. 8, which is generated by ANSYS®ICEM CFD. The grid is refined in the boundary layer and near the struts. Since the computational accuracy highly depends on the grid resolution, it is necessary to choose a grid size that is sufficiently fine to solve the flow domain accurately and small enough to save computational time. To analysis the grid sensitivity, a sequence of three grids is tested. The coarse grid, the fine grid, and the dense grid contain 1.0, 4.0 and 8.0 million cells, respectively. Typical value of y+ is less than 5 for most near wall cells since the enhanced wall treatment is used.

To determine the appropriate grid size and validate such a numerical approach involved in the paper, the experimental results are brought into comparison with the computational results. As exhibited in Fig. 9b and d, the computational limiting streamlines from the fine

Table 1 Geometrical parameters of the curved annular duct

$\Delta R/l_0$	r_1/l_0	R_1/l_0	r_2/l_0	R_2/l_0	h/l_0	w/l_0	l_c/l_0	l_3/l_0
0.41	0.72	0.82	0.32	0.56	0.17	0.10	0.60	0.24

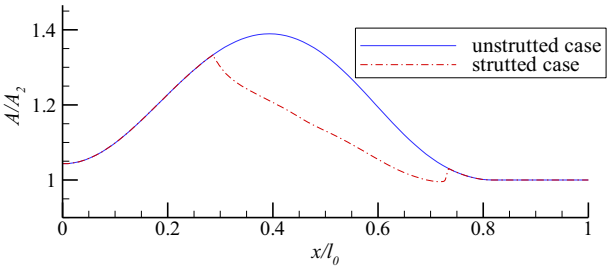

Fig. 5 Duct area distributions of the curved duct

and dense grids show good consistency with the experimental results, capturing the complicated flow pattern around the strut, whereas in Fig. 9a, the limiting streamlines calculated by the coarse grid fail to predict the separation lines (S_2) and (S_3) on the shroud surface, and (S_5) on the hub surface. In order to insure the accuracy and save computing resource, the fine mesh is selected in the following numerical investigations. In addition, the influence of rotation correction to the turbulence model is also discussed. The results acquired with and without rotation correction are compared in Fig. 9b and c. It can be easily found that, without the correction, the computational limiting streamlines on the shroud surface fail to capture the separation lines (S_2), while the hub-side case show little difference. Therefore, the rotation correction equips the Realizable k-ε model with a better capability in predicting the complicated secondary flow [22, 23]

4 Results and Discussion

4.1 Flow characteristics at a representative exit mach number

In order to acquire an overview of the flow structures within the curved duct, the detailed flowfield at a representative exit Mach number of 0.46 is analyzed at first.

First of all, it is necessary to discuss the inflow condition. It is widely accepted [7, 24, 25] that the Reynolds number based on the inlet duct height and mean flow velocity can be representative of the inlet boundary layer condition. Since the boundary layer trips are neglected in the experiment, the inflow Reynolds number is just around 1.0×10^5, less than that in reference [7] (Re=2.6×105), [24] (Re=2.5 ×105) and [25] (Re=2.5×105), in all

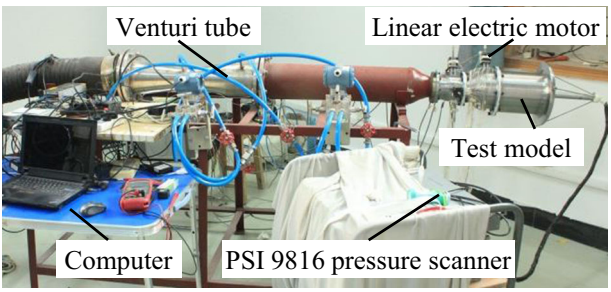

Fig. 6 Measurement and control system of the test

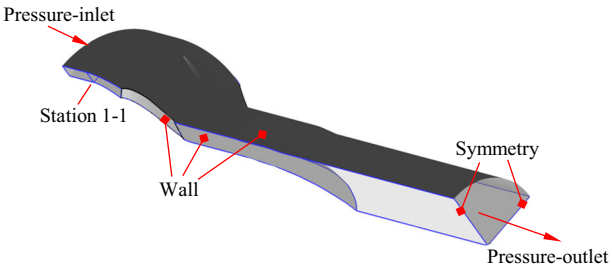

Fig. 7 Computational domain boundary conditions

of which the boundary layer trips are used. Figure 10 displays the total pressure profiles at station 1-1 obtained computationally and experimentally. According to the experimental results, the inlet boundary layers near the hub and the shroud are both approximately 1.5mm in thickness, occupying 15 % of the passage height. However, due to the absence of the boundary layer trips, the boundary layer status is still unknown, but likely not fully developed turbulence since the fully turbulent computational result presents a thicker boundary layer.

As shown in Fig. 11, the hub-side and shroud-side wall pressure distributions show remarkable differences. Next, the hub-side distribution is discussed. Across the first bend, a local low-pressure region is formed on the leeward side with a minimum static pressure coefficient (p/p_0) of 0.837. After that, the static pressure increases rapidly to a maximum value of 0.902 at the middle part of the duct. Whereafter, the static pressure decreases gradually in the subsequent part of the duct until a rapid drop appears at the second bend of the duct. In contrast, the shroud-side pressure distribution varies more violently. In the front part of the duct, the static pressure coefficient rises continuously to a maximum of 0.919. However, the situation is reversed in the aft part, where the flow experiences a substantial positive pressure gradient. The minimum static pressure coefficient at the second bend is as low as 0.766. Finally, the static pressure coefficient recovers to the level of the hub-side one at the duct exit through an adverse pressure gradient region.

Figure 12 presents the Mach number contours on two symmetric planes of typical circumferential positions. According to the contours on the symmetric plane of the flow passage as shown in Fig. 12a, the flow decelerates at the first bend of the duct and the local boundary layer grows rapidly. By contrast, the flow is accelerated in the second bend and the development of the boundary layer is suppressed remarkably. Since experiencing a higher favorable pressure gradient (seen in Fig. 11), the shroud-side boundary layer is much

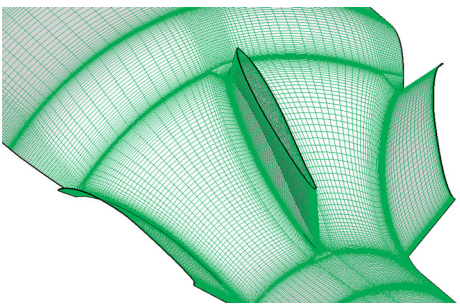

Fig. 8 Computational grids for the strutted curved annular duct

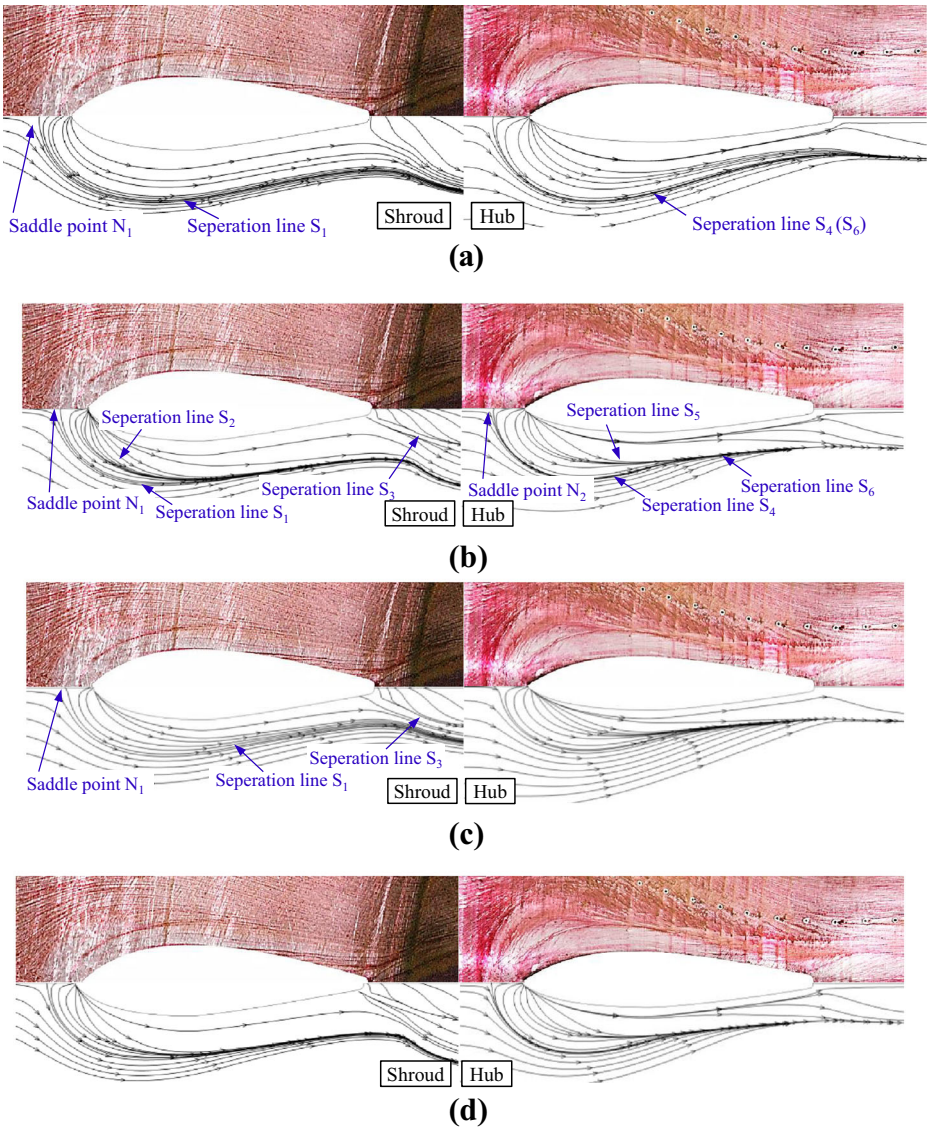

Fig. 9 Comparison of limiting streamlines on the shroud surface and hub surface from the computation and experiment at the representative exit Mach number of 0.46. (**a**) Coarse grid; (**b**) Fine grid-with rotation correction; (**c**) Fine grid-without rotation correction; (**d**) Dense grid;

thinner than the hub-side one, especially at the aft part of the annular duct. Moreover, two local high-velocity regions are generated near the hub at the first bend and near the shroud at the second bend, respectively, which adds the spatial non-uniformity of the flowfield. The flow details adjacent to the strut can be seen from the contours on the symmetric plane of the strut as shown in Fig. 12b. Due to the presence of the strut, apparent Mach number gradients appear near the leading edge and the trailing edge. In addition, slight flow separation can be found in the hub-strut corner.

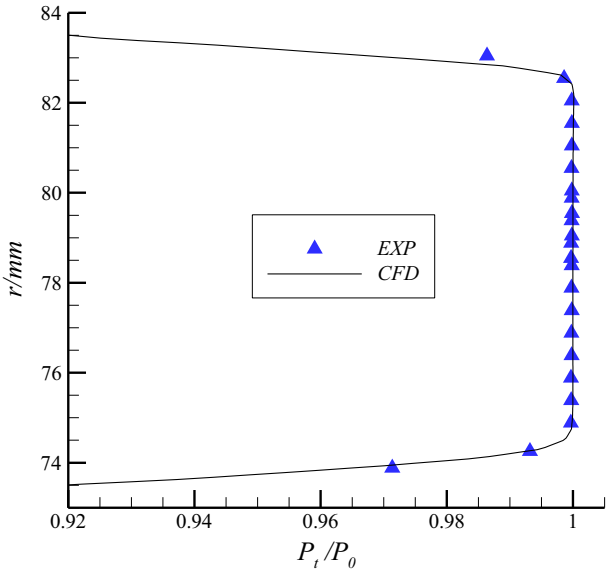

Fig. 10 Total pressure profile at station 1-1

To figure out the evolution of the internal flow structure more clearly under the interference of the struts, Mach number contours of five equally spaced cross sections are presented in Fig. 13. These five sections, which correspond to the strut leading edge position, the strut middle position, the strut trailing edge position, the duct exit position and a certain position downtream the duct exit, are marked with Section a-a, Section b-b, Section c-c, Section 2-2, Section d-d. When the flow reaches Section a-a, a significant Mach number gradient is induced by the strut leading edge. However, the boundary layers near the hub and the shroud still keep relatively uniform. At Section b-b, the corner boundary layers begin to shift away from the strut. The contour plots of Section c-c show that the low-momentum flow in the hub-side boundary layer accumulates further. Moreover, the strut trailing edge also brings

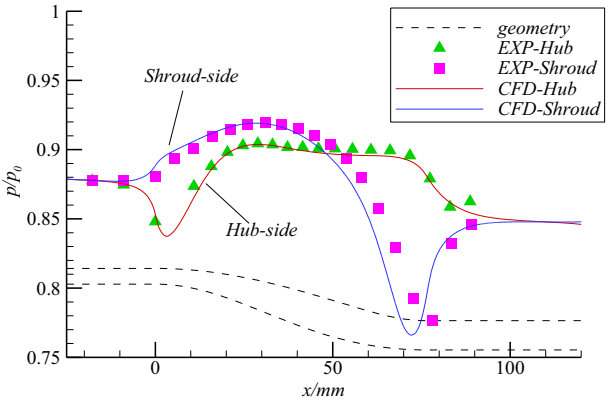

Fig. 11 Static pressure distributions along the hub and shroud surface

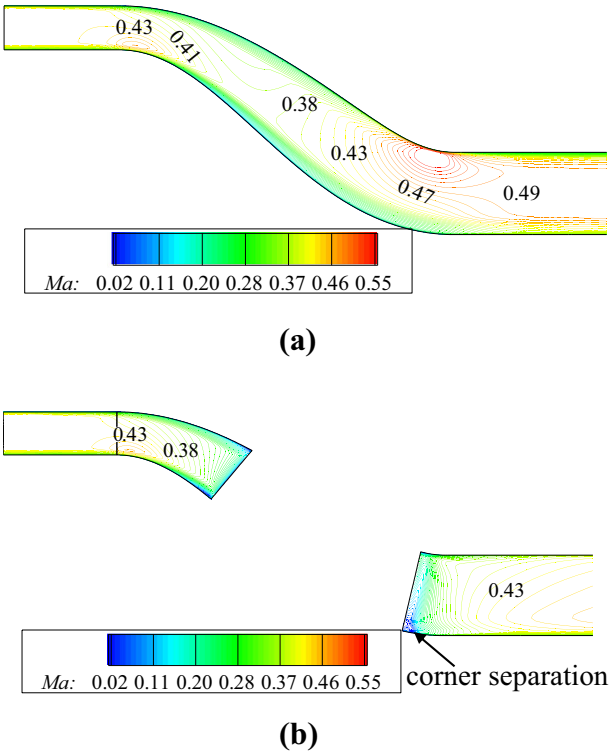

Fig. 12 Mach number contours on (**a**) the symmetric plane of the flow passage between two adjacent struts and (**b**) the symmetric plane of the strut

on the wake flow. Thereby, the flowfield influenced by the vortices and wake becomes even more complicated. When evolving downstream, the vortices and wakes both mix with the core flow and dissipate finally, leading to multiple low-energy regions, as shown by contours on Section 2-2 and Section d-d.

Figure 14 displays the total pressure contours on the exit of the curved duct (Section 2-2). Owing to the struts, several wakes come about and each is approximately 3 mm in width. Furthermore, low total pressure regions can be also observed clearly beside the wakes. According to the computational results, the total pressure recovery σ at the duct exit is 0.985.

4.2 Generation and evolution of the vortices

As mentioned above, the vortices are induced near the hub and the shroud under the effect of the struts, resulting in high total pressure loss. This section is devoted to shedding light upon the generation mechanism and evolution characteristics of the vortices.

Before analyzing the complicated flowfield with multiple vortices, it is worthwhile discussing the surface flow structures on the shroud (Fig. 9b left), hub (Fig. 9b right) and struts (Fig. 15) first. On the shroud, a typical horseshoe vortex forms ahead of the strut leading edge with a Saddle point (N_1). From this saddle point, a Separation line (S_1) emerges and wraps around the strut. After a rapid turn near the head of the strut, S_1 moves toward the

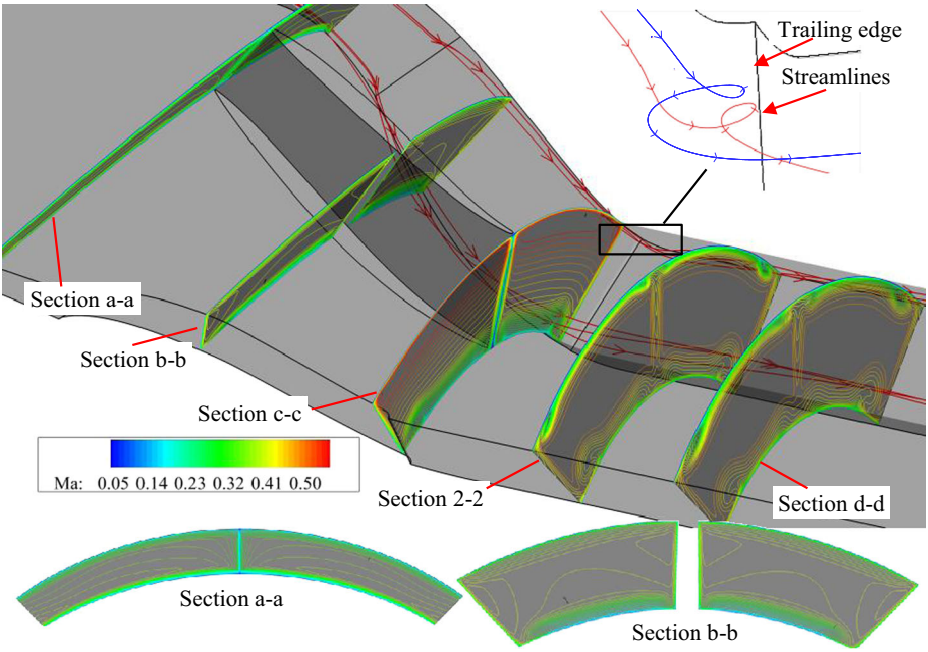

Fig. 13 Mach number contours at different sections along the flow passage

strut surface and merges with the successive Separation line (S_2). The coalescent separation line extends further and begins to diverge downstream the strut. In addition, another Separation line (S_3) originates from the trailing edge of the strut and develops with a large divergence angle. This flow phenomenon is quite similar to that observed by [20] and [26] in which S_3 is called "wake limiting streamline". The streamlines and wall shear stress lines shown in Fig. 13 and Fig. 9b (left) both indicate that there is a high concentration of vortices downstream the trailing edge of the strut. According to the wall shear stress lines shown in Fig. 9b (right), the flow pattern near the hub resembles that of the shroud. However, differences can still be detected after a careful inspection. Firstly, the Separation line (S_4) from Saddle point (N_2) is plumper than S_2. Secondly, the divergence angle of the Separation line (S_6) merged from S_4 and S_5 is much smaller downstream of the strut than that on the shroud. Finally, no wake limiting streamline can be observed near the trailing edge of the strut.

Fig. 14 Total pressure contours on the exit of the curved duct

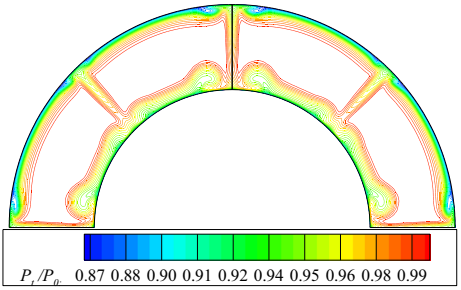

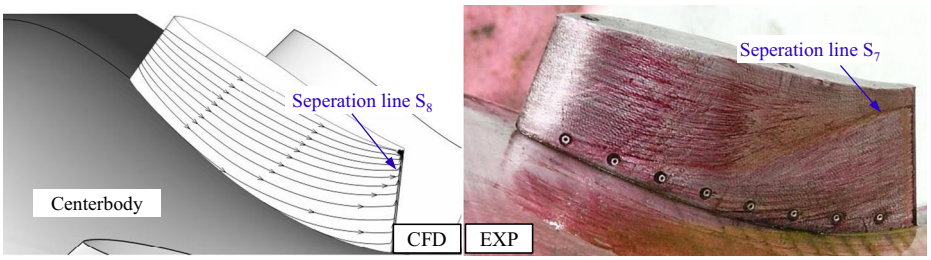

Fig. 15 Comparison of limiting streamlines from computation and experiment on the strut surface

According to the oil flow pattern on the strut surface shown in Fig. 15, one can note that the limiting streamlines turn outwards rapidly downstream the mid part of the strut and a Separation line (S_7) forms at its rear part. The radial migration of the limiting streamlines in Fig. 15 can be explained by the radial pressure gradient on the strut surface which is induced by the low-pressure region near the shroud of the second bend. For further explanation, Fig. 16 exhibits the surface pressure distributions along the section lines on 10 %, 50 %, and 90 % strut span, respectively, where the x-axis (l) represents the arc length. On the fore part of the strut surface, the discrepancy between the three pressure distributions is rather small. However, on the aft part of the strut surface, the static pressure distribution of the section line on 90 % strut span begins to plunge and a large pressure gradient along the radial direction comes into being.

In order to reveal the generation mechanism and evolution characteristics of the vortices, Fig. 17 shows secondary flow vectors on the five cross sections defined in Fig. 13. To display the motional trend of the secondary flow vectors more clearly, some necessary corresponding streamlines are added. The sections are rotated to the normal direction and z-axis and y-axis represent the spanwise direction and passage height direction, respectively. The characteristics of the secondary flow on each section are discussed as follows.

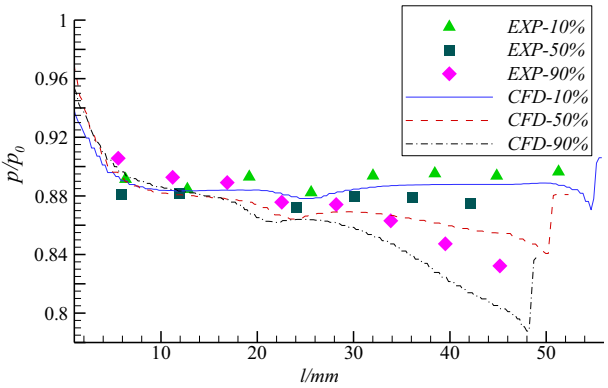

Fig. 16 Surface pressure distributions of different section lines on the strut surface

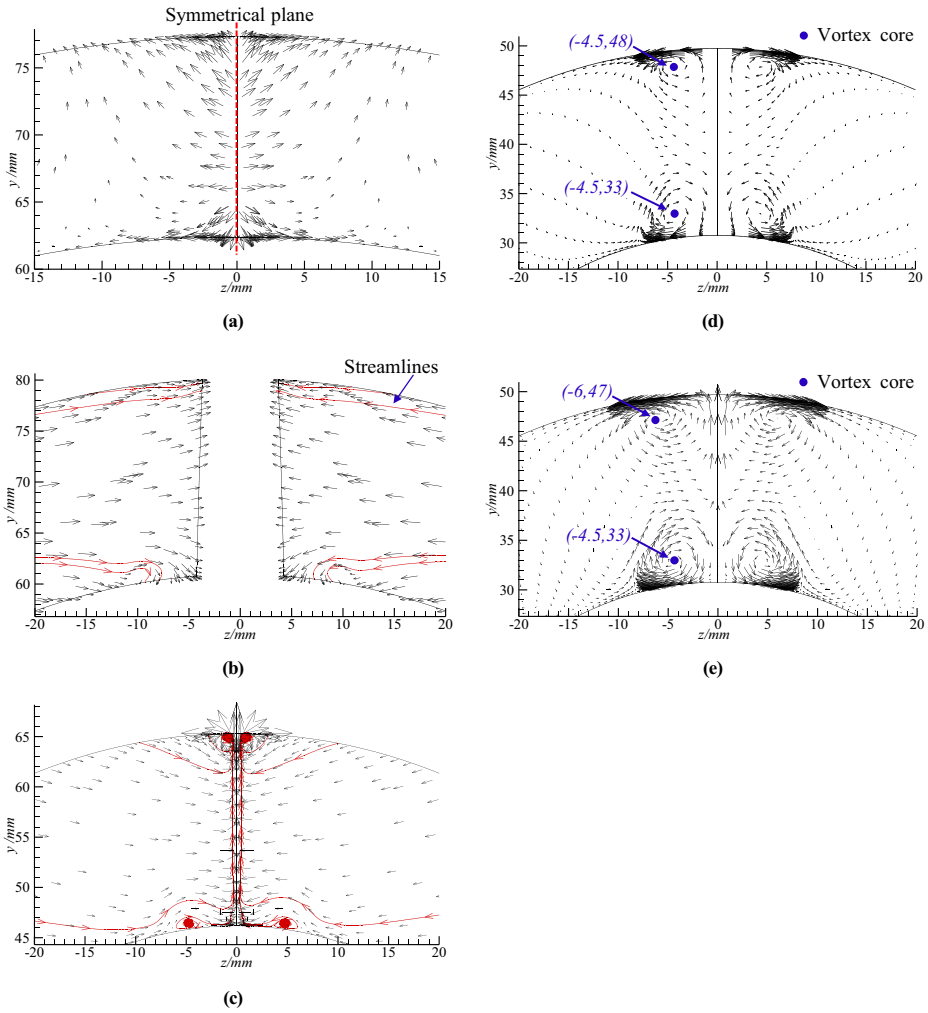

Fig. 17 Secondary flow vectors of (**a**) Section a-a, (**b**) Section b-b, (**c**) Section c-c, (**d**) Section 2-2 and (**e**) Section d-d

Section a-a When the flow reaches the strut leading edge (Fig. 17a), the streamlines passing through Section a-a are diverged towards left and right sides due to the blocking effect of the strut. The velocity of the airflow has also an overall positive y-component since the duct is bended inwards locally.

Section b-b As shown in Fig. 17b, the secondary flow turns back towards the strut surface at Section b-b to follow the surface of the strut. Actually, the surface pressure gradient on the strut along the streamwise direction also promotes the spanwise migration of the secondary flow. In addition, a counter-rotating vortex pair can be observed near the hub at about z= ±10 mm.

Section c-c According to Fig. 17c, after arriving at the strut trailing edge, the secondary flow still takes on a motion trend towards the symmetrical plane at Section c-c. At the same time, the secondary flow near the strut shifts towards the outer wall as influenced by the local low pressure region near the shroud. As a result, the flow accumulates near the shroud, forming a pair of vortices near the symmetrical plane. The migrating pathline of the vortices corresponds to the separation line of S_8 shown in Fig. 15. The vortex is also demonstrated by the streamline evolution in Fig. 13.

Section 2-2 At Section 2-2 (Fig. 17d), the counter-rotating vortices near the hub and shroud develop rapidly and obtain a much wider range of influence. In addition, it can be discerned clearly that the vortex pair near the hub is in the opposite direction of that near the shroud.

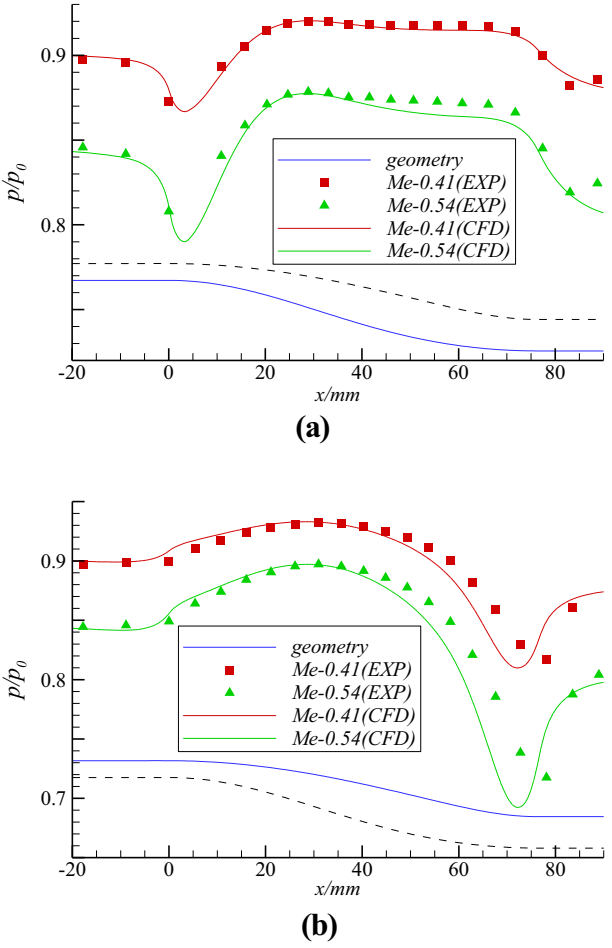

Fig. 18 Comparisons of surface static pressure distributions along (**a**) the hub and (**b**) the shroud at different exit Mach numbers

Section d-d At Section d-d, the vortices expand further and entrain more low energy flow. The position of the vortex core near the hub remains roughly unchanged. However, for the shroud-side vortex pair, the absolute value of z-coordinate of the vortex core increases apparently as compared with that on Section 2-2. That is, the shroud-side vortices are moving away from each other in the spanwise direction during their formation and transportation.

A summary can be made regarding the evolution of these vortices. The shroud-side vortex pair, whose path line corresponds to the Separation line S_3 shown in Fig. 9b (left), is generated at the trailing edge near the strut-shroud corner and travels downstream in a divergent way. By contrast, the hub-side vortices, which are firstly captured at Section b-b, move from Section c-c to Section d-d parallel and yield the horizontal separation line S_6. Since S_6 is the coalescent separation line of S_4 and S_5, the formation of the hub-side vortices can be traced back to the horseshoe vortices induced by the strut leading edge. That is, the generation mechanisms of the two vortex pairs shown on Fig. 17e are much different, which can be explained further as follows. Return to the strut-shroud corner flow, the horseshoe vortices are generated near the strut leading edge firstly, and soon the air flow near the shroud experiences a favorable pressure gradient. Therefore, the low momentum flow is accelerated again and the vortices are stretched longer and sped up in rotation, decreasing the influence region of the horseshoe vortices and quickening up their dissipation process. So small scale vortices can hardly be observed according to the secondary flow vectors. As a result, the shroud-side vortex pair on section d-d can be regarded to be unrelated with the horseshoe vortices. When it comes to the strut-hub corner flow, similarly, the horseshoe vortex system is generated near the strut leading edge. Subsequently, a remarkable adverse pressure gradient is imposed on the vortex system downstream the middle point of the strut due to the inward deflection of the hub surface, which intensifies the vortex system and increases the corresponding influence regions. Actually, the high pressure caused by the junction flow downstream the trailing edge of the strut also apparently contributes to the growing of the counter-rotating vortices near the hub, as shown in Fig. 17c and d.

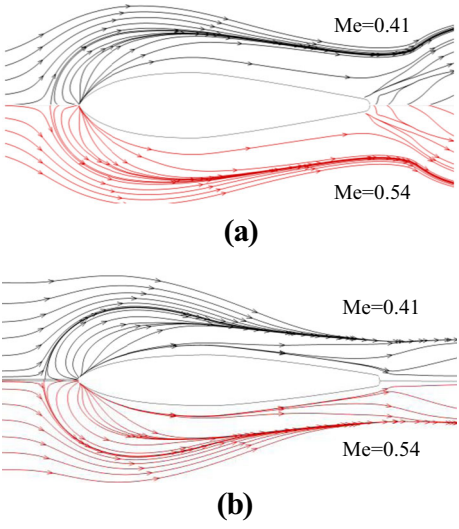

Fig. 19 Comparisons of wall shear stress lines of (**a**) the shroud surface and (**b**) the hub surface at different exit Mach numbers

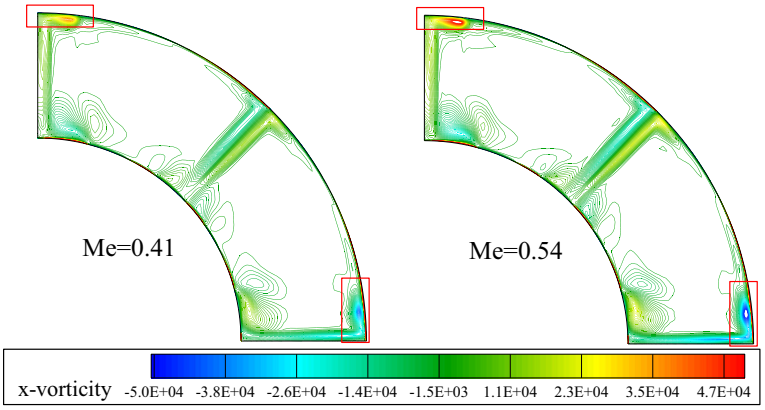

Fig. 20 Comparison of x-vorticity contours on the exit section at different exit Mach numbers

4.3 Effect of the exit mach number

To investigate the effect of the exit Mach number on the secondary flow characteristics, this part compares the flowfield within the curved annular duct at the exit Mach numbers 0.41and 0.54.

The comparison of the surface static pressure distributions is shown in Fig. 18. The trends are similar to that of M_e =0.46 in Fig. 11. As the exit Mach number increases, the static pressure decreases entirely. Accordingly, the pressure gradients near the hub of the first bend and the shroud of the second bend both get intensified, which implies that a larger exit Mach number will influence on the vortex characteristics more significantly.

Figure 19 presents the computational wall shear stress lines at different exit Mach numbers. According to the results, the flow structures are exceedingly alike and also similar to that of M_e =0.46. This indicates that the change of the exit Mach number can hardly

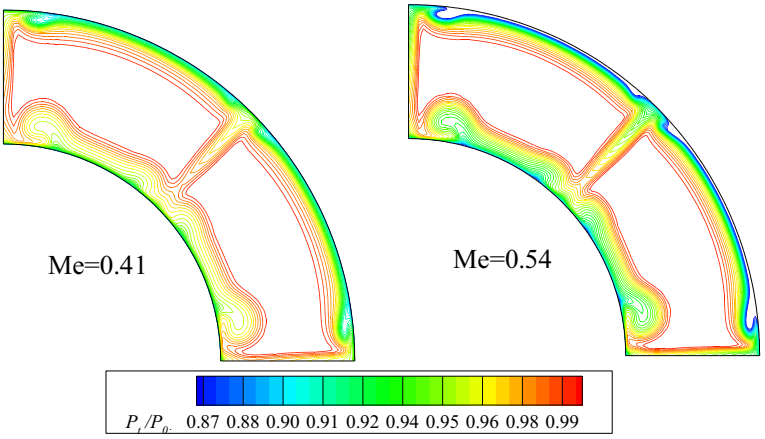

Fig. 21 Comparison of total pressure contours on the exit section at different exit Mach numbers

bring obvious impact on the flow patterns of the vortices. However, this alters the vortex intensity. As shown in Fig. 20, the x-vorticity magnitude of the shroud-side vortices of M_e =0.54 is higher than that of M_e =0.46, which indicates that the vortices near the shroud become stronger as the exit Mach number increases. Evidently, this is resulted from the larger adverse pressure gradient across the second bend.

Comparing the total pressure contours on the duct exit section shown in Fig. 21, it is not difficult to find that the stronger vortices bring on a more intense mixture with the core flow. Therefore, the total pressure recovery (P/P_0) of the vortical regions is lower in the case of M_e =0.54.

5 Conclusions

Combining the experimental and computational methods, this paper investigates the secondary flow characteristics within a curved annular duct with struts. Firstly, the flowfield at a representative exit Mach number of 0.46 is detailedly analyzed. Due to the curvature of the ducts and the variation of the cross-sectional area, large streamwise pressure gradients are generated cross the two bends. At the same time, under the interference of the struts, vortex pairs are formed in the vicinity of the hub and shroud. The streamwise pressure gradients significantly influence the vortex characteristics. When experiencing the positive streamwise pressure gradient, the low momentum flow gets accelerated and the vortices are stretched longer and sped up in rotation, diminishing the influence regions and augmenting the dissipation. On the contrary, the adverse streamwise pressure gradient facilitates the accumulation of the low momentum fluids and promotes the generation and evolution of the vortices.

Dominated by the above-mentioned flow mechanism, the hub-side and shroud-side vortices exhibit different characteristics due to the influence of different streamwise pressure gradients. The hub-side vortices evolve from the horseshoe vortices which are induced by the strut leading edge, whereas the shroud-side ones originate from the strut trailing edge. In addition, the vortices show different evolution characteristics. The hub-side vortices travel parallelly, while the shroud-side ones develop in a divergent way. As the exit Mach number increases, the streamwise pressure gradients get higher, imposing a more significant influence on the secondary flow characteristics. As a result, the vortices become stronger and the accompanying total pressure loss gets larger.

Acknowledgments This study is funded by the Fundamental Research Funds for the Central Universities through Grant No. 3082014NS 2014016 and the Priority Academic Program Development of Jiangsu Higher Education Institutions

References

1. Sorensen, N.E., Smeltzer, D.B.: Study of two axisymmetric inlets for mach 3.5. AIAA 1976-0204 (1976)
2. Wei, R.L.J., Sanders, B.W.: A new design concept for supersonic axisymmetric inlets. In: 38th AIAA/ASME/SAE/ASEE Joint Propulsion Conference & Exhibit, Indianapolis, Indiana, AIAA paper 2002-3775 (2002). doi:10.2514/6.2002-3775
3. Vittal, B.V.R., Tipton, D.L., Bennett, W.A.: Development of an advanced vaneless inlet particle separator for helicopter engines. J Propulsion Power **2**(5), 438–444 (1986). doi:10.2514/3.22926
4. Breitman, D.S., Dueck, E.G., Habashi, W.G.: Analysis of a split-flow inertial particle separator by finite elements. J Aircraft **22**(2), 135–140 (1985). doi:10.2514/3.45097

5. Al-Faris, E.F., Saeed, F.: Design and optimization method for inertial particle separator (ips) system. In: 12th AIAA/ISSMO Multidisciplinary Analysis and Optimization Conference, British Columbia Canada, AIAA Paper 2008-6066 (2008). doi:10.2514/1.40921
6. Smith, C.F.: Six sigma methods applied to an inlet particle separator design. In: 13th AIAA/ISSMO Multidisciplinary Analysis and Optimization Conference, Texas, America, AIAA Paper 2010-9398 (2010). doi:10.2514/6.2010-9398
7. Ortiz, D.C., Miller, R.J., Hodson, H.P.: Effect of length on compressor inter-stage duct performance. In: Proceedings of ASME Turbo Expo 2007: Power for Land, Sea and Air, Montreal, Canada, ASME paper GT2007-27378 (2007). doi:10.1115/GT2007-27752
8. Walker, A.D., Barker, A.G., Carrotte, J.F.: Integreted outlet guide vane design for an aggressive s-shaped compressor transition duct. In: Proceedings of ASME Turbo Expo 2011, British Columbia, Canada, ASME Paper, GT2011-45627 (2011)
9. Wu, Y.D., Li, B., Chen, Y.Y.: Automated design optimization and experimental validation for intermediate casing duct of aeroengine. In: Proceedings of ASME Turbo Expo 2013: Turbine Technical Conference and Exposition, Texas, USA, ASME Paper GT2013-94137 (2013). doi:10.1115/GT2013-94137
10. Axelsson, L.U., Osso, C.A., Cadrecha, D.: Design, performance evaluation and end wall flow structure investigation of an s-shaped intermediate turbine duct. In: Proceedings of ASME Turbo Expo 2007: Power for Land, Sea and Air, Montreal, Canada, ASME paper GT2007-27650 (2007). doi:10.1115/GT2007-27650
11. Wallin, F., Arroyo, O.C., Johansson, T.G.: Experimental and numerical investigation of an aggressive intermediate turbine duct: part ihflowfield at design inlet conditions. In: 26th AIAA Applied Aerodynamics Conference, Honolulu, Hawaii, AIAA paper AIAA 2008-7055 (2008). doi:10.2514/6.2008-7056
12. Marn, A., Gottlich, E., Malzacher, F., Heitmeir, F.: Comparison between the flow through an aggressive and a super-aggressive intermediate turbine duct. ISABE, 2009–1259 (2009)
13. Doerffer, P., Flaszynski, P., Magagnato, F.: Streamwise vortex interaction with a horseshoe vortex. Int. J. Therm. Sci. **12**(4), 304–309 (2003). doi:10.1007/s11630-003-0035-7
14. Paik, J., Escauriaza, C., Sotiropoulos, F.: On the bimodal dynamics of the turbulent horseshoe vortex system in a wing-body junction. Phys. Fluids **19**(4), 1–20 (2007). doi:10.1063/1.2716813. 045107
15. Gand, F., Deck, S., Brunet, V., Sagaut, P.: Flow dynamics past a simplified wing body junction. Phys. Fluids **22**(11), 1–16 (2010). doi:10.1063/1.3500697. 115111
16. Andoh, M., Motosuke, M., Honami, S.: Interaction of longitudinal vortex with horseshoe vortex. In: 39th AIAA Fluid Dynamics Conference, San Antonia, Texas, AIAA paper 2009-4176 (2009). doi:10.2514/6.2009-4176
17. Hu, S.Z., Zhang, Y.F., Zhang, X.F., Vlasic, E.: Influence of inlet swirl distributions on an inter-turbine duct-part i: casing swirl variation. In: Proceedings of ASME Turbo Expo 2007, British Columbia, Canada, ASME Paper, IGTI GT2011-45554 (2011). doi:10.1115/GT2011-45554
18. Zhang, Y.F., Hu, S.Z., Zhang, X.F., Vlasic, E.: Influence of inlet swirl distributions on an inter-turbine duct- part ii: hub swirl variation. In: Proceedings of ASME Turbo Expo 2011, British Columbia, Canada, ASME Paper, IGTI GT2011-45555 (2011). doi:10.1115/GT2011-45555
19. Bailey, D.W., Britchford, K.M., Carrotte, J.F., Stevens, S.J.: Performance Assessment of an Annular S-Shaped. Duct. J. Turbomach **119**, 149–156 (1997)
20. Sonoda, T., Arima, T., Oana, M.: The influence of downstream passage on the flow within an s-shaped duct. J Turbomach **120**(4), 714–722 (1998). doi:10.1115/1.2841782
21. Sonoda, T., Arima, T., Oana, M.: The effect of inlet boundary layer thickness on the flow within an annular s-shaped duct. J Turbomach **121**(3), 626–634 (1999). doi:10.1115/1.2841361
22. Jones, W.P., Launder, B.E.: The prediction of laminarization with a two equation model of turbulence. Int. J. Heat Mass Transf. **15**(2), 301—314 (1972)
23. Zhao, Y., Wang, G.Y., Huang, B., Hu, C.L.: Applications of a curvature correction turbulent model for computations of unsteady cavitating flows. In: International Symposium of Cavitation and Multiphase Flow (ISCM 2014). doi:10.1088/1757-899X/72/2/022006
24. Britchford, K.M., Manners, A.P., McGuirk, J.J., Stevens, S.J.: Measurement and Prediction of Flow in Annular S-Shaped Ducts. Exp. Therm. Fluid Sci **9**(2), 197-205 (1994)
25. Naylor, E.M.J., Ortiz, D.C., Miller, R.J., Hodson, H.P.: Optimization of Nonaxisymmetric Endwalls in Compressor S-Shaped Ducts. In: Proceedings of ASME Turbo Expo 2008: Power for Land, Sea and Air, Berlin, Germany, ASME paper GT2008 (2008)
26. Karim Abdulla-Altaii, A., Raj, R.S.: Secondary flow development downstream of a blade endwall corner. In: ASME 1994 International Gas Turbine and Areoengine Congress and Exposition, Hague, Netherland, ASME Paper, No.94-GT-459 (1994). doi:10.1115/94-GT-459